Proceedings of the 21st ICSMGE, Vienna, Austria, 14 – 19 June 2026. Pistrol, Adam & Schweiger (eds.)
Published by: ÖGG, Austrian Society for Geomechanics, Salzburg, Austria, ISBN 978-3-9503898-4-5
https://doi.org/10.53243/ICSMGE2026-510

DEM simulation of 1D compression tests on pumice sands using bonded element model

Denny Budiman, Rolando P Orense
University of Auckland, Auckland, New Zealand, dbud.341@aucklanduni.ac.nz

ABSTRACT: Pumice sand is a type of volcanic-derived sand commonly found on the North Island of New Zealand. It has a unique characteristic compared to ordinary hard-grained sands due to its porous, lightweight, and crushable characteristics. This study simulates 1D compression tests conducted on dense and loose New Zealand pumice sand in Discrete Element Modelling (DEM) using PFC3D V6.0. The pumice particles are simulated as spherical bonded agglomerates comprising individual balls with 0.2 mm in diameter. The agglomerates are created by bonding the individual balls using the Linear Parallel Bond contact model, while the Linear contact model is used for the interactions between balls. The DEM strength parameters from previous single particle crushing test simulations are used and calibrated to match the existing laboratory results by comparing the vertical stress-strain response of the specimens subjected to increasing vertical stress up to a load of 1740 kPa. With increasing vertical stress, force networks are developed between intact agglomerates and are transferred to the neighbouring agglomerates upon particle crushing. As the vertical stress increases, the input boundary energy into the system also increases, mostly stored as strain energy or dissipated through friction, damping, or lost when a bond is broken. Investigation into the energy distribution shows that a portion of the strain energy is released when a particle is crushed. In contrast, increases in friction and damping energy dissipation are observed, which may be linked to the increasing possible contacts with the particles spawned from the particle crushing.

KEYWORDS: Pumice sand, Discrete Element Method (DEM), agglomerates, particle crushing, stress network, energy distribution.

1 INTRODUCTION

New Zealand has been a hotspot for volcanic activity in the past due to its location being on the boundary between two tectonic plates. From these series of volcanic activities, volcanic materials were scattered across many of its regions. Pumice sand is an example of a volcanically-derived soil in New Zealand that has different characteristics from the ordinary hard-grained sand; its particles are porous and lightweight, easily crushable, and compressible. This causes pumice sand to be problematic from a construction point of view. Furthermore, limited information is available regarding its liquefaction susceptibility/behaviour because it is less commonly encountered than its hard-grained sand counterparts and the expensive and time-consuming laboratory and field tests.

With the advancement of computational capabilities, recent studies often utilised computational simulations with appropriate constitutive models, such as the Discrete Element Modelling (DEM) (e.g. Bahmani & Orense 2021; Ciantia et al. 2015; Wang & Yan 2012). In contrast to the more commonly known Finite Element Method (FEM), DEM simulates all the individual particles in the simulation along with their interactions (O'Sullivan, 2014), allowing observations on particle scale, including the development of the particles' movements, rotations, and contact forces. The interactions between the particles are governed by the adopted contact models, which can include a cement-like bond between particles, allowing the creation of particles with various shapes, sizes, and internal void distributions.

Using the capabilities of DEM, this study investigates the micromechanical behaviour of pumice sand during 1D compression tests performed by Wesley (2007) using PFC3D v6.0 (Itasca Consulting Group Inc., 2018). The crushable pumice sand particles are simulated as bonded agglomerates, which are contained within rigid boundaries representing the 1D compression apparatus.

2 CRUSHABLE PARTICLE SIMULATION

When simulating particle crushing in DEM, two simulation methods are often employed: the fragment replacement method, where the crushed particle is replaced with unbonded smaller particles when the particle crushing criteria are met, or the agglomeration method, where the crushable particle is created as bonded smaller particles. While the former has been proven to be more practical for large-scale models due to the lower number of particles generated in the simulation and satisfactorily captures the macromechanical behaviour of crushable material (e.g. Bahmani & Orense 2021; Ciantia et al. 2016), the latter has been shown to be able to investigate the micromechanical behaviour and development of particle crushing (Wang and Yan, 2012). For this reason, the agglomeration method has been used in this study.

2.1 *Single particle crushing strength*

The DEM parameters for the agglomerates are calibrated to existing single particle crushing test data of Japanese (Kikkawa 2016) and New Zealand pumice sands (Bahmani 2021) between 1 mm and 8 mm. The Japanese and New Zealand pumice sands have similar mechanical properties, surface shapes, surface texture, and surface voids (Pender et al., 2015).

During these tests, the particles are sandwiched between two rigid plates and are subjected to compression stress, which is converted into tensile stress within the particle. Particle crushing occurs when this tensile stress exceeds the particles' strength, which can be indirectly expressed as in Equation (1), where d = diameter of the particle; and F = diametrical force.

$$\sigma = \frac{F}{d^2} \tag{1}$$

The average tensile strength, σ_f, of a particle is a function of the particle size, d, where the particle size has an inverse relationship to the average crushing strength (Lee, 1992). Similarly, Orense et al. (2013) observed that both hard-grained sand and pumice sand particles tend to have a trend of decreasing crushing strength with increasing particle size.

In addition to the variation in strength with changing particle size, particles of a given size may also exhibit variation in strength, which can be attributed to statistical variations in flaws within the particles (McDowell & Bolton, 1998). This variation in strength is often expressed using the Weibull statistics (Weibull, 1951) through the Weibull modulus (m). The Weibull modulus decreases as the variability in strength increases (McDowell & Amon, 2000). For instance, crushable Quiou sand has m between 1.2 and 1.9 (McDowell & Amon,

2000); silica sands have m between 1.8 and 3.0 (Nakata et al., 2001); stone, brick, chalk, and pottery have $m \approx 5$; and engineered ceramics have an $m \approx 10$ (Ashby & Jones, 1986).

Equations (2)-(3) show the Weibull statistical model for spherical soils, where Ps = survival probability; m = Weibull modulus; d = diameter of the particle; d_0 = reference diameter; σ_c = applied tensile stress; and σ_{c0} is the characteristic stress that causes 37% of the particles to survive at d_0 (referred to as the 37% tensile strength).

$$Ps(d) = \left[exp \left[- \frac{d^3}{d_0^3} \left(\frac{\sigma_c}{\sigma_{c0}} \right)^m \right] \right] \quad (2)$$

$$Ps(d_0) = \left[exp \left[- \left(\frac{\sigma_c}{\sigma_{c0,d0}} \right)^m \right] \right] \quad (3)$$

In a recent study, the authors processed the single particle crushing test data of New Zealand pumice sand and proposed m = 1.3-1.9 for New Zealand pumice sand between 1 mm and 8 mm, and a modulus (m_{size}), representing the variation in strength between particle sizes, as $m_{size} \approx 4.23$. Using m_{size}, the 37% tensile strengths of other agglomerate sizes are determined, and the variation in strength within a given particle size is calculated using Equations (4)-(6) (Ciantia et al., 2019), where σ_{lim} = crushing strength; $\bar{\sigma}_{average}$ = average crushing strength; Var = variability in strength; and $X_{p,0,1}$ = a random variable with a Gaussian distribution with a mean of zero and a standard deviation of one.

$$\bar{\sigma}_{average} = \sigma_0 \Gamma(1+1/m) \quad (4)$$

$$\bar{\sigma}_{average}(d) = \bar{\sigma}_{average}(d_0) \left(\frac{d}{d_0} \right)^{-3/m} \quad (5)$$

$$\sigma_{lim}(d) = \bar{\sigma}_{average}(d) * f(1+Var*X_{p,0,1}) \quad (6)$$

2.2 *Porous particle generation*

The crushable pumice sand particles are simulated as agglomerates, which consist of bonded ball elements with a diameter of 0.2 mm. The Linear contact model has been chosen to represent the normal and shear interaction between balls, while the Linear Parallel Bond contact model has been used to bond the agglomerates. The bonds behave similarly to a cement-like contact point between balls that can resist tension and shear but offer no resistance against rotation. The agglomerates are spherical in shape, with a rolling resistance introduced between them to represent the effect of particle shape. This rolling resistance reduces the sliding and rotation of the agglomerates by resisting the moments acting on the particles, while keeping the computational time lower. An example agglomerate is shown in Figure 1.

Due to the nature of the agglomerate method simulation, all the particles needed in the simulation are present from the beginning of the simulation. This means that the mass is conserved within the system throughout the simulation. Another benefit of this method is that asperity crushing, particle chipping, and particle splitting on the agglomerates are unique and fully dependent on the acting forces on the agglomerates.

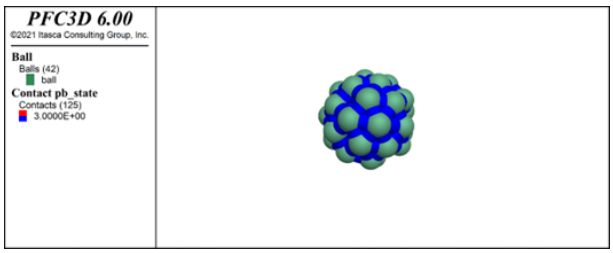

Figure 1. A DEM model of a porous agglomerate.

2.3 *Energy distribution in PFC3D*

The Linear contact model in PFC3D allows for three energy partitions to be recorded: the strain energy (E_s), which is the energy stored in the linear springs; slip energy (E_μ), which is the total energy dissipated through friction; and dashpot energy (E_β), which is the energy dissipated by the damping (Itasca Consulting Group Inc., 2018).

These energy partition recordings can then be combined with the built-in FISH function, which allows monitoring, accessing, and recording the data at any time during the cycling. Additional energy partitions, such as the boundary (input) energy (E_{bound}), body work from gravity (E_g), lost stored strain energy when a bond breaks (E_{bond_break}), and the kinetic energy (E_k) can also be recorded (Itasca Consulting Group Inc., 2018). In this study, the simulations are conducted under a zero-gravity condition ($E_g = 0$).

To satisfy the energy conservation law, the energy distribution is assumed to follow Equation (7) at any time during the cycling (Wang and Yan, 2012). In a system where the energy is perfectly conserved, the plastic energy (i.e. sum of E_s, E_μ, E_β, E_{bond_break}, and E_k) will equal the input boundary energy.

$$Ebound + Eg = Es + E\mu + E\beta + Ebond\_break + Ek \quad (7)$$

3 1D COMPRESSION SPECIMEN PREPARATION

3.1 *Specimen generation*

A 4 mm high and 12 mm in diameter cylindrical 1D compression specimen is generated in this study using the boundary contraction method. The specimen has a maximum particle size to height (h/d_{ratio}) of about 1.7. This h/d_{ratio} has been selected to minimise the number of agglomerates spawned. While this h/d_{ratio} is considered low, other studies (e.g. Ciantia et al., 2015) managed to capture the mechanical behaviour and grading evolution of their specimens with a similar ratio.

To generate a double porosity specimen, a procedure similar to that of Ciantia et al. (2016) is performed while assuming the same specific gravity, i.e. $G_s = 1.77$, that Wesley (2007) adopted, plus some adjustments to account for using the agglomerate method. The model originally contains individual balls with sizes matching the targeted particle size distribution from Wesley (2007), as shown in Figure 2. The model is then cycled until the balls are in equilibrium, and the porosity of this ball formation is recorded as the initial apparent porosity (n^*). These individual balls are then replaced with agglomerates of the same size as each ball, creating a double porosity specimen. Trials and errors were carried out for n^* until the final porosity (n) satisfactorily matches Wesley's inferred porosity (n^+). Note that Ciantia et al. (2016) adopted a porosity difference (Δn) of -0.15, which is slightly different from this study. Δn is a correction factor for the difference between the exact and approximated intragranular porosities due to an assumed constant internal porosity. In this study, Δn has been calculated

from the porosity difference pre- and post-agglomerate replacement. The full methodology can be found in their study. Table 1 summarises the adopted and target porosities for both dense and loose specimens, while Table 2 shows the DEM parameters for this simulation.

After the specimen with the desired porosity has been generated, load stages up to 1740 kPa are applied to the specimen. The stress-strain development, particle crushing occurrences, and energy distribution are recorded throughout the simulation.

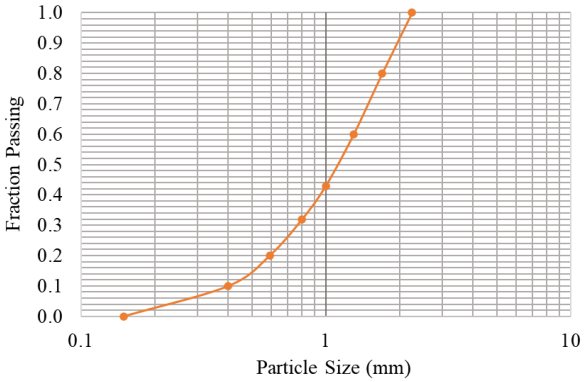

Figure 2. Particle size distribution for the 1D compression model.

Table 1. 1D compression specimens' target porosities.

Specimen type	n^*	n^{inter}	Δn	n	n^+
Dense	0.46	0.23	-0.16	0.63	0.59
Loose	0.50	0.25	-0.15	0.66	0.65

Table 2. DEM parameters.

Parameter	Symbol	Value	Unit
Solid density	ρ	2490	kg/m^3
Contact normal stiffness	*ln_kn*	100,000	N/m
Contact stiffness ratio	*krat*	2.27	-
Bond stiffness ratio	*pb_krat*	2.27	-
Bond effective modulus	*pb_emod*	140e6	Pa
Bond tensile strength	*pb_ten*	12e6	Pa
Bond cohesion	*pb_coh*	12e6	Pa

4 RESULTS

The specimen was loaded vertically by applying load stages while keeping all the other boundaries stationary. Figure 3 shows the axial strain-vertical stress response from the DEM simulation in comparison to the work by Wesley (2007). The DEM simulation predicted a similar response to the laboratory result, with an acceptable overestimation at the lower stress due to some particles initially not being in contact with each other. Therefore, the models and calibrated parameters are considered satisfactory for the purpose of micromechanical observations in this study.

4.1 *Contact force network development*

By saving the simulation results between the stages, the contact force network can be exported, as shown in Figure 4 to 6 for the dense specimen. These figures are the specimen's vertical cross-sections (passing through the centre) at 430 kPa, 860 kPa, and 1740 kPa vertical loads, respectively, with the magnitude of force experienced by the balls shown as the grey balls in the background, overlaid with the contact force network. As the magnitude of the force increases, the darker these balls appear. Similarly, the contact force network becomes thicker and brighter as the contact force increases.

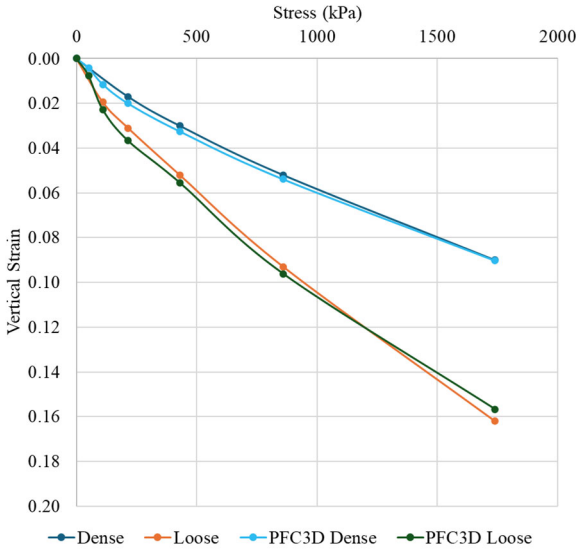

Figure 3. 1D compression test result: vertical stress-axial strain.

The area marked with a red rectangle in these figures highlights the progression of particle crushing with increasing load on a relatively large agglomerate cluster, indicated by the brightening of the grey balls. Initially, it appears that the contact force chains form a kind of network that connects uncrushed particles, as seen in Figure 4. Although the simulation was terminated at a moderate stress level (i.e. 1740 kPa), vertical stress networks have formed at a lower stress level and seem to start growing in other directions towards the end of the simulation. As the particles undergo particle crushing, this network is erased from the crushed particle, causing stress redistribution and concentration surrounding the crushed particle, as shown in Figure 5 and Figure 6.

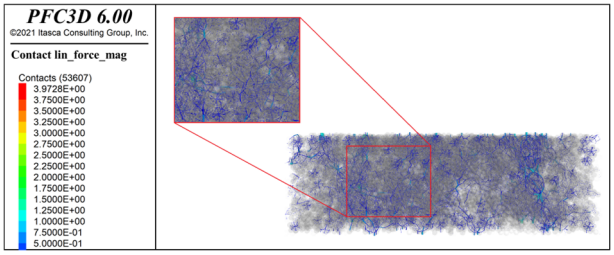

Figure 4. Contact force cross-section for dense specimen at 430 kPa.

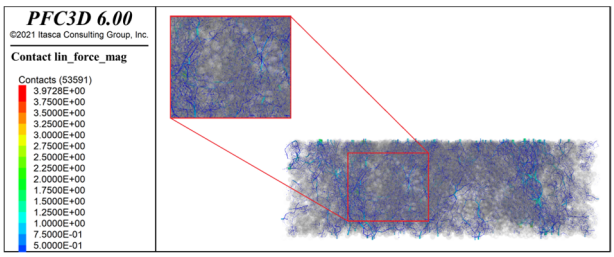

Figure 5. Contact force cross-section for dense specimen at 860 kPa.

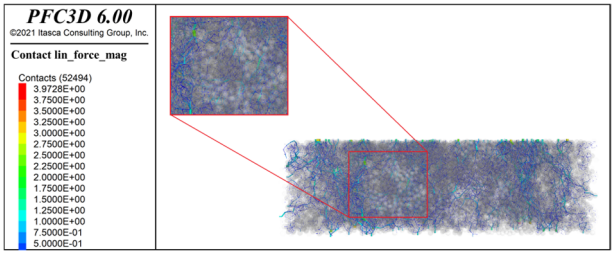

Figure 6. Contact force cross-section for dense specimen at 1740 kPa.

4.2 *Particle crushing*

The occurrences of particle crushing are indicated by the bond breakages between the ball elements during the simulations. When a bond breaks, the balls associated with this bond can detach from the main agglomerate, creating new, smaller agglomerates. Depending on how many balls detach from the parent agglomerate, it can be classified as asperity crushing, particle chipping, or major particle splitting. Due to computational and time limitations, the particle crushing investigation was only performed on the dense specimen.

During the cycling process, the fragmentation function in PFC3D has been used to keep track of particle crushing. When the fragmentation function is enabled, PFC3D calculates and keeps track of the number of bonded agglomerates and their volumes. Each of the bonded agglomerates is considered a fragment. This function is called every time a bond breakage is triggered during the computational cycling. Using this function, the volume changes in the agglomerates can be monitored every time this function is called.

Figure 7 shows the development of particle crushing with increasing vertical stress and the ball loss from each bond breakage for the dense specimen. The agglomerates are classified into varying size categories based on how many balls are left in the agglomerate after the bond breakage. The number of balls lost after the bond breakage is displayed on the secondary Y axis. Similarly, Figure 8 shows the percentage of ball loss for the dense specimen.

Comparing these two figures reveals that up to a stress level of approximately 430 kPa, the majority of bond breakages are asperity crushing, indicated by a minimal percentage of ball loss. As the stress level increases to 860 kPa, significant particle chipping, particle splitting, and even greater asperity crushing occur. These particle crushings are dominated by the smaller particles up to 1.3 mm. Finally, when the vertical stress increases to 1740 kPa, more particle crushing occurs as expected. At this stress level, particle chipping and splitting are observed on several larger particles between 1.3 mm and 2.3 mm. These observations are in agreement with McDowell & Bolton (1998), where the coordination number governs over the lower crushing strength, which causes smaller particles with lower coordination numbers to continue crushing and provide cushion for the larger particles.

These figures also reveal that all bond breakages occur immediately after load application and during the stress ramp-up in the specimen. During this period, both particle crushing and particle rearrangement contribute to the induced strain. After the stress within the specimen matches the applied load, the subsequent strain in the specimen is dominated by the particle rearrangement.

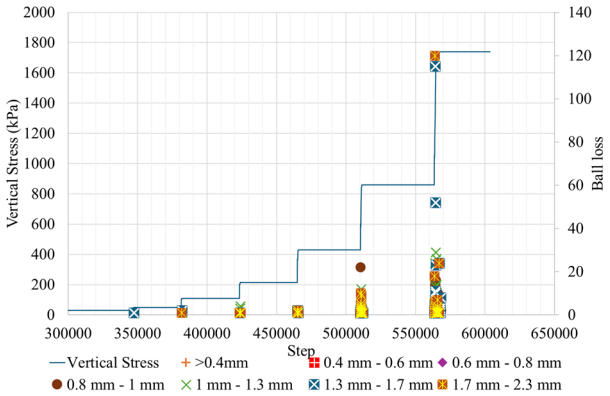

Figure 7. Number of balls lost from particle crushing (dense).

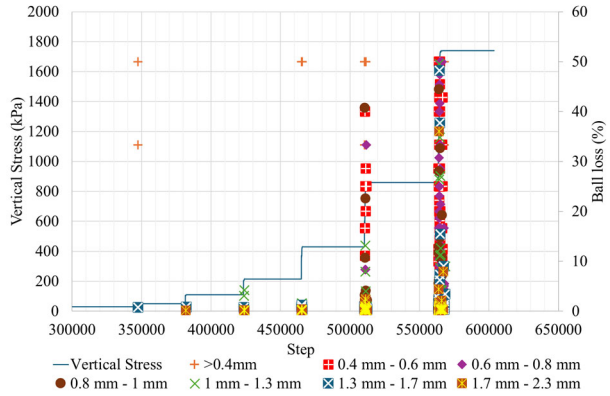

Figure 8. Percentage of balls lost from particle crushing (dense).

4.3 *Energy distribution*

The energy distribution during the simulation is captured in every calculation cycle using the FISH function. While the kinetic energy is present in the system and can be recorded, post-processing this energy is extremely difficult due to the unclear initially available kinetic energy in the system at the beginning of load application. The magnitude of the kinetic energy at the end of each load application is deemed low enough to be ignored in this study.

Figure 9 and 10 show the normalised energy distribution and incremental energy distribution, respectively, of the dense specimen. Similarly, Figure 11 and Figure 12 illustrate the same energy distributions for the loose specimen. The vertical dotted lines indicate the strain at which a loading stage is applied. Comparing the normalised energy distribution for the dense and loose specimens, it is observed that the dense specimen generally has a higher proportion of the strain energy. In comparison, the loose specimen has a higher proportion of friction and damping energy. This agrees with the observation by Wang & Yan (2012), which can be attributed to the dense specimen having more contact between particles, inducing more strain energy, while the loose specimen has more voids that allow the particles to readjust and slide against each other, causing more energy to be dissipated through friction and the damping mechanism dissipating the energy from particle movement.

Also observed from these plots is that abrupt drops in the strain energy and an increase in friction and damping energy generally happen with the application of a new loading step, followed by a gentler decrease in strain energy with increasing

strain. The downward trend in strain energy may be associated with particle rearrangement and potential particle crushing. This can be explained by investigating the vertical stress-axial strain development in Figure 13. In contrast to Figure 3, where it connects the data points of the final strain values after the application of the load stages, Figure 13 shows the development of strain due to the applied vertical stress. It should be noted that although it seems in Figure 13 that the next load stage is applied immediately after the previous stress has been reached, a sufficient number of cycles are performed between load stages until a satisfactory stress equilibrium is reached, as shown in Figure 7 and 8.

When a new load stage is applied to the specimen, the particles undergo particle rearrangement and potentially particle crushing while the stress within the specimen rises. During these stress ramp-ups, the specimen undergoes most of the strain recorded. For example, the dense specimen's strain goes up from 5.4% to 9% after the application of the 1740 kPa load. However, significant numbers of particle crushing are also recorded during the same load ramp-up period, as shown in Figure 7 and 8. Therefore, these drops in strain energy may be associated with the earlier particle crushing immediately after load application, and the downward trend is potentially induced by the later particle crushing and particle rearrangement during the stress ramp-up.

As for the energy loss from bond breakages, a negligible amount of this energy has been recorded, similar to the observation by Wang & Yan (2012). While the energy loss during particle crushing itself is negligible, it promotes changes in the soil fabric by creating new, smaller particles that increase the friction and damping dissipation from more soil particle interactions.

Figure 10 and 12 show the incremental energy of the loose and dense specimens, respectively. The boundary energy indicates the total energy input, and the plastic dissipation sums up the total dissipated energy from the friction, strain, and bond break energy. These plots show PFC3D's ability to adequately conserve energy within the system, shown by the plastic dissipation being in close range to the boundary energy. The strain energy dominates in both dense and loose specimens, followed by friction and damping energies. The energy dissipated by bond breakages is small, but it is observable that more bond break energy is recorded in the dense specimen due to more agglomerates and contacts being present. Similarly, the friction and damping energy seem more significant on the loose specimen due to the agglomerates being freer to rearrange and readjust.

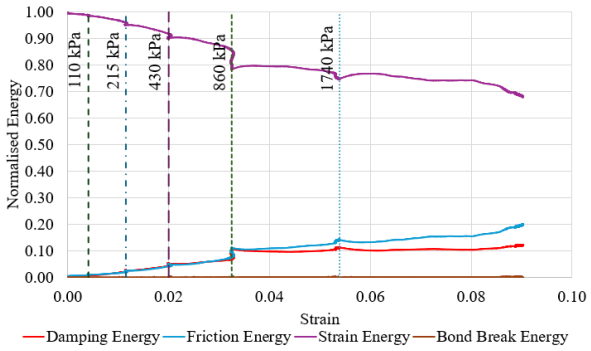

Figure 9. Normalised energy distribution (dense).

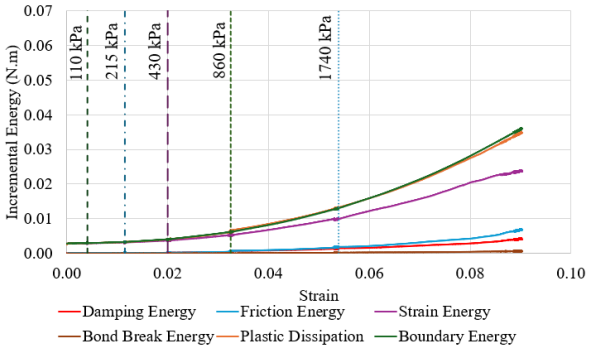

Figure 10. Incremental energy distribution (dense).

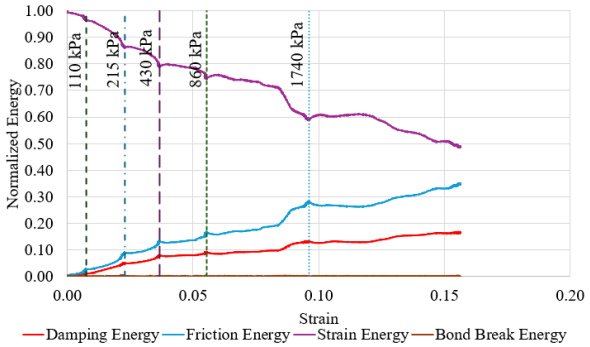

Figure 11. Normalised energy distribution (loose).

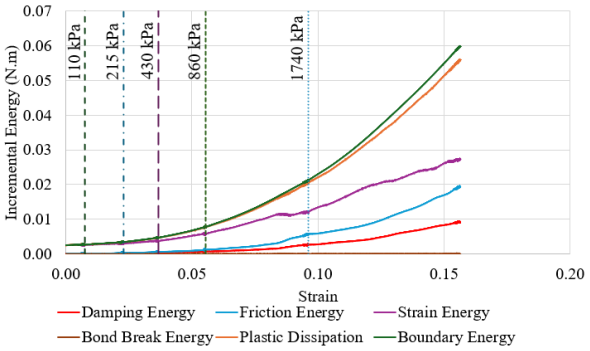

Figure 12. Incremental energy distribution (loose).

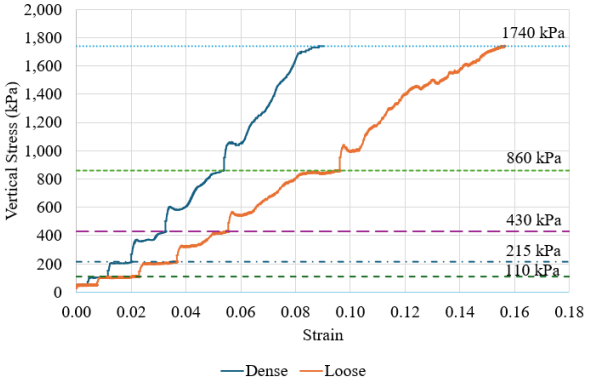

Figure 13. Vertical stress-axial strain development.

5 CONCLUSIONS

This study investigated the micromechanical behaviour and energy distribution of crushable pumice sand during a 1D compression test using the Discrete Element Method (DEM) simulation. The specimen was 4 mm in height and 12 mm in diameter, with the pumice sand simulated as bonded agglomerates. The Weibull statistics were used to represent the inherent variability in particles' crushing strength.

When calibrating the model to an existing laboratory 1D compression result, the DEM results satisfactorily captured the vertical stress-strain response. The main observations from the simulations are summarised as follows:

1. The vertical force chain network formed early within the specimen in response to load application, which propagated in other directions as the load increased. Localised force chains were erased when the particle was crushed and became concentrated in its surroundings.
2. Asperity crushing and particle chipping took place from the medium stress level, and major particle splitting became more frequent with increasing stress level. Smaller particles were more prone to particle crushing due to a lower coordination number, which acted as a cushion for the larger particles.
3. The FISH function was used to investigate energy distribution during the simulation. The dense specimen was found to have a larger strain energy proportion compared with the loose specimen due to more contacts between the particles, while the loose specimen tended to dissipate larger friction and damping energy in general due to more voids within the specimen, which allowed the particles to move and readjust.
4. The occurrences of particle crushing were concentrated during the load ramp-up immediately after a new load application. During these load ramp-ups, drops and a downward trend of strain energy were observed, which may be attributed to the particle readjustment and particle crushing.
5. The energy loss when a particle breaks was minimal, but it induced the generation of new particles and contacts between particles, which tended to increase the friction and damping dissipation.

This study showcased the ability of DEM to perform detailed macroscale observations on laboratory simulations. The authors intend to use the simulation methodology in this study as a framework for other laboratory tests (e.g. K0 and CPT chamber tests). Understanding the behaviour of pumice and its underlying mechanism of particle crushing at the microscale aids in explaining the unique macroscale behaviour of pumice sand during such tests, for example, the similar cone resistance response of pumice sand to ordinary hard-grained sand as observed by Wesley (2007). It is hoped that this information will help the development of more refined design methods and soil investigation techniques when dealing with pumiceous soils.

6 REFERENCES

Ashby, M.F. and Jones, D.R.H., 1986. *Engineering Materials 2*. Elsevier.

Bahmani, S.H., 2021. Discrete element modelling of highly crushable pumice sand. *PhD Thesis*, University of Auckland.

Bahmani, S.H. and Orense, R.P., 2021. DEM simulation of 1-D compression test on pumice sand. In: *NZGS Symposium 2021*.

Ciantia, M.O., Arroyo, M., Butlanska, J. and Gens, A., 2015. DEM modelling of a double-porosity crushable granular material. In: *Geomechanics from Micro to Macro - Proceedings of the TC105 ISSMGE International Symposium on Geomechanics from Micro to Macro, IS-Cambridge 2014*. Taylor and Francis - Balkema. 269-274.

Ciantia, M.O., Arroyo, M., Butlanska, J. and Gens, A., 2016. DEM modelling of cone penetration tests in a double-porosity crushable granular material. *Computers and Geotechnics*, 73, 109-127.

Ciantia, M.O., Arroyo, M., O'Sullivan, C., Gens, A. and Liu, T., 2019. Grading evolution and critical state in a discrete numerical model of Fontainebleau sand. *Géotechnique*, 69(1), 1-15.

Itasca Consulting Group Inc., 2018. *PFC - Particle Flow Code, Ver. 6.0*.

Kikkawa, N., 2016. Strength and deformation properties of porous granular material and proposal for a ground investigation method focusing on elasto-plastic deformation and crushing of its particles. In: *KAKENHI Grant-in-Aid for Young Scientists (B) Final Report.* [online] Available at: <https://kaken.nii.ac.jp/en/grant/KAKENHI-PROJECT-23760448/>.

Lee, D.-M., 1992. Angles of friction of granular fills. *PhD Thesis*, University of Cambridge.

McDowell, G.R. and Amon, A., 2000. The application of Weibull statistics to the fracture of soil particles. *Soils and Foundations*, [online] 40(5), 133-141.

McDowell, G.R. and Bolton, M.D., 1998. On the micromechanics of crushable aggregates. *Géotechnique*, 48, 667-679.

Nakata, Y., Kato, Y., Hyodo, M., Hyde, A.F.L. and Murata, H., 2001. One-dimensional compression behaviour of uniformly graded sand related to single particle crushing strength. *Soils and Foundations*, [online] 41(2), 39-51.

Orense, R.P., Pender, M.J., Hyodo, M. and Nakata, Y., 2013. Micro-mechanical properties of crushable pumice sands. *Géotechnique Letters*, 3(APRIL/JUN), 67-71.

O'Sullivan, C., 2014. *Particulate Discrete Element: A Geomechanics Perspective*. Spon Press.

Pender, M.J., Orense, R.P. and Kikkawa, N., 2015. Japanese and New Zealand pumice sands: Comparison of particle shapes and surface void structures. In: *Geomechanics from Micro to Macro*. 1111-1116.

Wang, J. and Yan, H., 2012. DEM analysis of energy dissipation in crushable soils. *Soils and Foundations*, 52(4), 644-657.

Weibull, W., 1951. A statistical distribution function of wide applicability. *Journal of Applied Mechanics*, [online] 18(3), 293-297.

Wesley, L.D., 2007. Geotechnical characteristics of a pumice sand. In: *Characterisation and Engineering Properties of Natural Soils*. 2449-2473.